Towards fully printed memristive elements: a-TiO_2 electronic synapse from functionalized nanoparticle ink

Journal:	*ACS Applied Electronic Materials*
Manuscript ID	el-2019-007012.R1
Manuscript Type:	Article
Date Submitted by the Author:	19-Nov-2019
Complete List of Authors:	Salonikidou, Barbara; University of Surrey, Electrical & Electronic Engineering Takeda, Yasunori; Yamagata University - Yonezawa Campus, Research Center for Organic Electronics Le Borgne, Brice; University of Surrey, Electrical & Electronic Engineering England, Jonathan; University of Surrey, Electrical & Electronic Engineering Tokito, Shizuo; Yamagata University Faculty of Engineering Graduate School of Science and Engineering , Sporea, Radu; University of Surrey, Electrical & Electronic Engineering

Towards fully printed memristive elements: a-TiO_2 electronic synapse from functionalized nanoparticle ink

Barbara Salonikidou[1], Yasunori Takeda[2], Brice Le Borgne[1], Jonathan England, Shizuo Tokito[2] and Radu A. Sporea[1]*

[1]Advanced Technology Institute (ATI), Faculty of Engineering & Physical Sciences, University of Surrey, Guildford, GU2 7XH, UK

[2]Research Center for Organic Electronics (ROEL), Yamagata University, 4-3-16 Jonan, Yonezawa, Yamagata 992-8510, JAPAN

ABSTRACT

Electronic devices that emulate bio-functionalities, such as synaptic plasticity, present a promising route to versatile and energy-efficient neuromorphic computing systems. As the demand for rapid-prototyping and environmentally-friendly fabrication of such devices rises, there are significant incentives toward finding solutions for low cost materials and flexible

deposition techniques. The development of printed electronic devices is still at an infant stage, presenting a timely opportunity to investigate material robustness and routes to overcoming fabrication obstacles towards fully printed electronic synapses. In this work, a low power, fully printed Ag *(200 nm)/*a-TiO_2*(80 nm)*/Ag *(160 nm)* memristive device is demonstrated. The first electrical characterization of early devices exhibits biomimetic properties with an indication of activity-dependent plasticity. The active material is derived from a simplified nanoparticle ink formulation developed in-house. The ink characterization confirms that the formulation fulfils the criteria for efficient jetting while exhibiting a dwell time of 4 months. Additionally, the common detrimental fabrication issues of layer cracks and control over uniformity here are both overcome. The ink optimization and the investigation of the electrical framework under which the memristive element responds synaptically present a favorable approach to alternative fabrication methods for future neuromorphic electronics.

KEYWORDS: printed; electronics; memristive; a-TiO_2 ink formulation; artificial synapse

INTRODUCTION

The brain is one of the most functionally complex and resource efficient organs in the human body. The source of the brain's dexterity is primarily based on its synaptic functionalities; a wondrous and far from fully-explored area. In neuroscience it is widely accepted that the synaptic efficacy, or synaptic strength *(w),* that controls a neuron's firing conditions, is critical for signal communication and information processing. It governs the neuronal activity through excitation or inhibition of the post-synaptic potential, [1] thus is vital for memory functions and

consequently for learning.[2] The key feature of interest of the synaptic strength is its plastic variation, in other words its activity-dependent variation over time.[3] In more detail, the stimulation of a synapse by a train of impulses results in a long-term or short-term modification of the synaptic strength depending on both the timing of the trigger arrival and the rate of stimulation. Tetanic stimulation (persistent stimuli of high rate) tends to produce a high rate of substance transmission (neurotransmitters and proteins) [3] that typically results into long-term potentiation/depression (LTP/LTD).[4] Longer time intervals between the trigger impulses, however, leave time for the synapse to transition to its relaxation state and result in short-term potentiation/depression (STP/STD).[5,6] It is also worth noting that, in cases of elevated excitability or chronic depression, homeostatic plasticity takes place to retain stability and to prevent the synapse from breakdown.[7]

To date, minimally structured electronic devices such as memristive elements[8,9] that emulate real synapses are the most suitable candidates for versatile and power-efficient computing paradigms. The imitation of these pivotal functionalities presents a major challenge today in the field of neuromorphic computing. In the last decades, memristive devices that are based on metal oxides have gathered much attention due to CMOS technology compatibility[10,11] and to their biomimetic switching characteristics.[12] One of the most well-studied active materials with reported memristive behavior in solid-state thin films is titanium dioxide (TiO_2).[13] However, its crystalline (c-TiO_2) forms: anatase, brookite, rutile[14] are mainly deposited by physical vapor deposition (PVD) or atomic layer deposition (ALD) at temperatures over 400 °C.[15] These techniques are lacking in both energy and cost efficiency. In contrast, the amorphous TiO_2 (a-TiO_2) can be formed at lower temperatures, below 150 °C.[16–18] This enables TiO_2 deposition

through solution-based techniques of lower complexity. Attempts have been made at fabricating bio-inspired electronic devices through low-cost fabrication techniques that are mainly based on spin-coating and drop-casting.[19–21] Unfortunately, these techniques lack control of areal uniformity and they usually require a separate additive and/or subtractive fabrication step.[22,23]

Recently, much attention is focused on inkjet printing (IJP), which is a candidate for the most promising unconventional fabrication method. The IJP technology aids the burgeoning field of flexible electronics to expand and progress. This additive fabrication technique is one of the most advantageous solution-processed based methods due to rapid prototyping capability, low material waste[24] and potential 3D patterning. IJP is a technique of lower cost and lower ecological impact compared to photolithography-based process, mainly due to the absence of material-etching chemicals. It is a non-contact technique and masks are not required. Within IJP, the least material-consuming and most commonly used operation mode is the drop on demand (DoD).[25] During DoD, a driving voltage in the form of pulsed signals is applied to the cartridge that is filled with the solution-ink. In this way, piezo-electrically induced drop ejection takes place and a small amount of individual ink droplets, in the order of picolitres, are deposited on the target substrate. The deposition and patterning are under direct computer control. Additionally, IJP deposition on a wide range of substrates[24] is feasible due to low temperature treatment and the option of rheology tuning through ink formulation. However, the adjustment of fluid rheology is not a predefined process and varies significantly depending on the active material. Features such as consistency and robustness in terms of rheological fluid characteristics are also far from established and ink related physics and chemistry remain key

challenges today.[26] Consequently, to advance to the state of manufacturing functional printed devices with an acceptable yield, the jetting and practical fabrication obstacles of IJP, along with ink durability, require addressing. The present work is concentrated on the investigation of these critical parameters in solution-processed a-TiO_2.

One of the most common fabrication drawbacks of solution-based TiO_2 is the development of cracks that subsequently result in leakage currents, and consequently to device failure.[19,27] To our knowledge, even though research has been carried out to overcome this limitation,[28] none is concerned with a-TiO_2 nanolayers that meet the IJP fabrication requirements for memristive elements. Additionally, reports on solution rheology and jetting characteristics are scarce, especially where related to ink formulation that maintains the key parameters within the specifications for the given IJP system.

In this project, Ag/a-TiO_2/Ag memristive devices with ~ 90 µm x 100 µm active area and nanoscale thickness are developed through DoD IJP using a functionalized ink developed and optimized in-house. The solution-ink is fully characterized, in terms of nanoparticle and Z number (viscosity, surface tension, density) determination, values that enclose vital information on jettability. The pH of the ink is not investigated here as it has minimal influence in DoD jetting performance.[26] The outcomes are within the acceptable range for effective printing and the final device is crack-free with well coverage and cell-to-cell thickness uniformity. Electrical characterization is conducted on early devices and the results indicate that both short-term and long-term potentiation with trigger timing-dependent characteristics are potentially feasible with the developed, fully-printed devices.

Electrical characteristics of TiO2

From the electrical perspective, memristive devices based on c-TiO_2 require an initial electroforming step in order to facilitate resistive switching (RS).[29,30] During electroforming, a high voltage is applied to the anode of the pristine c-TiO_2 device, breaking its crystal structure in a controlled manner and causing the creation and movement of oxygen vacancies (V_o) within the active layer,[29] and notably their arrangement into a conductive bridge[18,30] (an oxygen deficient interconnection)[31] across the electrodes, that consequently shifts the device from a high resistance state (HRS) to a low resistance state (LRS). Conversely, in devices based on a-TiO_2, the high electroforming voltages are not for resistive switching (RS) induction.[32] The RS does not emanate from a predefined pattern in this case due to the amorphous phase, but it is prone to more spontaneous state transitions. This probabilistic behavior could be suppressed through V_o doping control, a promising but laborious option.[33,34] Alternatively, the RS accuracy could be neglected and instead, the trend of the switching, in terms of event-driven variations in resistance, a characteristic that remains unaffected, could be exploited. Ultimately, the evolution of the resistive state (or the change in synaptic strength over time), is the feature that underpins both volatile (short-term) and non-volatile (long-term) memory functionality. The electrical framework that defines the trend of the switching should provide an insight into the underlying mechanism. Understanding it in depth is essential for the implementation of synaptic plasticity, which still requires significant investigation.

Electrical analysis of memristive devices usually entails performing current-voltage sweeps.[8,13] Alternatively, a biomimetic approach could be followed by applying voltage pulses[35], thus

characterizing the device by its current response over time. In this report, an attempt is made to understand and exploit the printed electronic synapse's behavior by keeping a constant voltage pulse amplitude and varying its timing characteristics.

EXPERIMENTAL SECTION

Device Fabrication: The samples consist of the following layers: polymer coating layer/Ag/a-TiO_2 /Ag/Teflon fabricated on glass substrates. Before the deposition of the bottom electrode, the substrates are cleaned with acetone, isopropanol and methanol followed by an ultrasonic bath clean with acetone and final rinsing with acetone and isopropanol. They are dried off with a N2 blow gun. Devices are fabricated via a sequence of layer deposition from bottom to top. For the bottom and top electrodes, in the first device, a Nanosilver ink is used (Ag NPs dispersed in ethanol, Kunshan Hisense Electronics Co., Ltd), while in the second device, a silver nanoparticle ink in hydrocarbon-based solution (NPS-JL, Harima Chemicals) was used. These were deposited through inkjet printing (IJP) (Fujifilm Dimatix DMP-2800 series) and sintered on a hot plate at 120 °C for ~ 20 min. The active layer is deposited through Fujifilm Dimatix in first sample and through a dispenser (Musashi Engineering ML-808GX) in second sample. In both cases, the synthesized ink is used as the active material (see the following section). In Fujifilm Dimatix, for all the printing steps DoD method and a single nozzle is used with a DMCLCP-11610 cartridge (10pL nominal droplet volume). The printing frequency is set at 2.0 kHz for the active ink and 1 kHz for the Ag, and the cartridge temperature was set at 30 ℃ and 40 ℃, respectively. In both cases, the printed active layers are left in air, under ambient conditions, for 30 min before

annealing on a hot plate at 80 °C for 10 min in air. Finally, the active area of the devices are encapsulated with Teflon (AF1600X, Dupont, Wilmington, DE, USA), dissolved in Fluorinert (FC-43, 3M Company, Maplewood, MN, USA) to 1 wt%.[36] The final active area of first device is ~ 150x90 μm^2 and of second ~ 150x180 μm^2.

Ink preparation/Formulation: For synthesis, a capping agent is added (1 ml of glacial acetic acid, HOAc) to the reaction matrix of (a) 1.26 ml of Ti (IV) isopropoxide (TTIP 97%, Sigma Aldrich), which is employed as a trace metal basis for the synthesis and used as received, and (b) 10 ml of 1-methoxy-2-propanol. After an overnight stirring in ambient conditions, the mixed compound is ultrasonicated for 30 min and filtered through 2 µm PTFE filter. For viscosity adjustment, ethylene glycol ($(CH_2OH)_2$) is added (1:1 vol %), followed by 30 min stirring under ambient conditions. In the first device, the jetting parameters of voltage and frequency are set at 22 V and 2 Hz, respectively with a drop spacing set to 30 µm. In the second device, a dispenser is used with a ⌀ 0.1 mm metal needle (brass with Ni plating) for the deposition. A pressure of 10 kPa is used for droplet ejection. In both samples, the printing head and sample holder temperatures are fixed at 30 °C.

Materials Characterization: The derived nanoparticle suspension-ink was characterized via dynamic light scattering using the Zetasizer Nano ZSP (Malvern Instruments Ltd. UK). The mean particle diameter and polydispersity index (PDI) are recorded. The measurements are performed at 25 °C without any prior sample preparation. The ink viscosity is determined using a DV3T Brookfield rheometer and the surface tension is measured on a Theta (Biolin Scientific) instrument. The deposited active layers are analysed by XPS, on a K-Alpha + spectrometer

(ThermoFisher Scientific Instruments, East Grinstead, UK). XPS spectra are acquired using a monochromated Al KaX-ray source (hv=1.486,6 eV) with an X-ray spot of ~ 400 µm radius. Survey spectra are acquired employing a Pass Energy of 200 eV. High resolution, core level spectra for all elements are acquired with a Pass Energy of 50 eV. All spectra are charge-referenced against the C1s peak at 285 eV to correct for charging effects during acquisition. Quantitative surface chemical analyses are calculated from the high resolution, core level spectra following the removal of a non-linear (Shirley) background. The manufacturer's Avantage software is used, which incorporates the appropriate sensitivity factors and corrects for the electron energy analyzer transmission function.

The morphology of the resulting layers is characterized using a Dektak XT (Bruker) profilometer and cross-section Scanning Electron Microscopy (SEM). The cross-section microscopy is conducted with a FEI Nova Nanolab and images are taken with a Tescan FERA3 Dual Beam for layer uniformity and thickness characterization. Before the milling process, using the Ga+ beam, Pt protective layers are deposited, assisted by electron (Pt-EBID, beam characteristics: 5keV and 0.4 nA) and ion (Pt-IBID, beam characteristics: 30 keV and 0.3 nA) beams. Cross-sections were then performed with the Ga+ beam (30 keV, 0.50 nA).

Electrical Characterization: The I-t measurements are conducted by using a Keithley 4200-SCS semiconductor parameter analyzer and a Wentworth probe station. For all the measurements, the top Ag electrode is biased, while the bottom Ag electrode is grounded, unless otherwise specified. The compliance current was set to 10 mA. The amplitude of voltage input steps was fixed at +1V and the pulse durations for each case can be found in the main text.

RESULTS AND DISCUSSION

Active Ink Characterization

The in-house formulated ink-solution for the active layer is based on Ti (IV) isopropoxide and 1-methoxy-2-propanol as the main solvent using a simplified combination of the sol-gel[37] and the Pechini methods[38] that does not incorporate an aqueous precursor or require a high temperature (see Experimental Section), unlike processes used elsewhere.[16,22,39,40]

The nanoparticle ink is characterized through dynamic light scattering (DLS). The measurement shows that the nanoparticles are mostly within a relatively narrow size distribution around 36 nm in diameter with some smaller, in the range of 10 nm (**Figure 1**a). The Z number is calculated to be approximately 2.9, according to the equation[41]:

$$Z = \frac{(\alpha \cdot \rho \cdot \gamma)^{\frac{1}{2}}}{\eta}$$

where, α is the diameter of the printing orifice (here, 21.5 μm), ρ is the ink density (~ 1070 kg/m^3), γ is its surface tension (~ 32 mN/m) and η is its viscosity (~ 9 mPa s). The resulting Z value falls well within the jettability range of 1 to 10.[42,43] Values smaller than 1 indicate high viscosity with low jetting probability, while values larger than 10 indicate low viscosity and can result in uncontrollable spontaneous jetting.

An X-ray photoelectron spectroscopy (XPS) measurement is performed to analyse the chemical composition of the deposited active film after its annealing. The results show a binding energy at 458.79 eV (15.34 %), which is attributed to the core level Ti $2p_{3/2}$ of Ti^{4+} state (**Figure 1**b).[44,45]

These findings correlate with the existing reports on sol-gel a-TiO_2 films.[44,46,47] It should be noted that the samples are annealed at significantly lower temperatures (~ 80 °C) compared to those required for crystalline TiO_2,[45] thus the most favorable phase here for TiO_2 is the amorphous one. The XPS survey (see **Table S**1, for the concentration of the elements in Supporting Information) shows the presence of carbon (C 1s peak at 284.8 eV) which arises due to adventitious carbon (C-C), thus is not correlated with the composition of the developed nanoparticles. The C-C contamination is expected as the sample was not cleaned or otherwise prepared before the XPS measurement. Apart from the minor concentration (0.43 %) of fluorine (F, at 689.32 eV), other elements are not apparent.

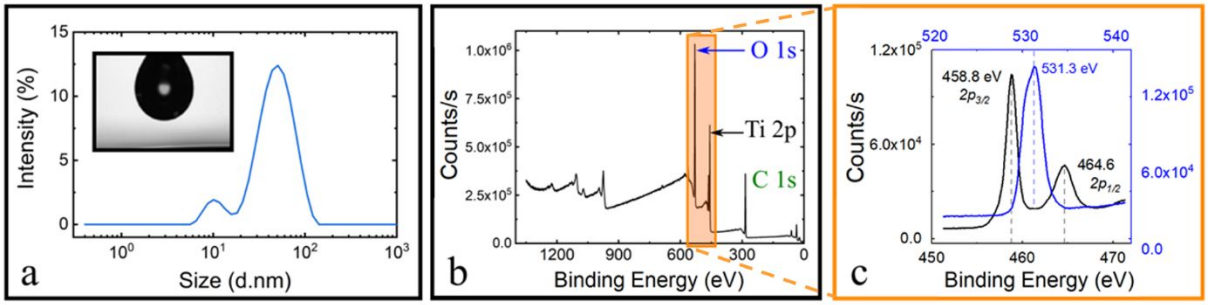

Figure 1. a) DLS measurements of 1-methoxy-2-propanol-based Ink. The graph presents the mean value of nanoparticles diameter (nm). The inset shows the respective droplets during surface tension measurements. b) XPS Survey of the a-TiO_2 active layer and c) the corresponding Ti_{2p} (black) and O_{1s} scan (blue) (the graphs are presented separately in Supporting Information **Figure S**2).

In this work, the synthesis takes place under ambient conditions, and does not require an autoclave and H_2O insertion, a process believed to cause nanoparticle agglomeration.[48] The

addition of ethylene glycol as a second solvent induces the enhancement of nanoparticle dispersion and the reduction of agglomerations. The presence of nanoparticle agglomerations often leads to a skinning effect during ink ejection (the formation of crust on the cartridge head surface) that results in clogging of the nozzles. The same property of improved dispersion can also be observed in 2-propanol-based ink, by following the same synthesis (see **Figure S**1 in Supporting Information). Additionally, the high boiling points of 1-methoxy-2-propanol and ethylene glycol (190 °C and 120 °C respectively) result in slower evaporation rate than in the case of 2-propanol and ethanol,[49] further mitigating the probability of the skinning effect. When synthesis follows recipes from literature, it produces an unstable solution with a presumably incomplete reaction which leads to nozzles clogging after a few uses, limiting cartridge lifetime and making jetting unreliable. However, in the present work, the functionalized ink developed in-house does not lead to notable clogging, extending considerably its lifetime to four months. Additionally, the derived film presents an amorphous nature with minimum residual elements. While it should be noted that limited reports exist on inks durability, as the inkjet printing is still in an infant stage;[50] the present work demonstrates promising results towards enabling the inkjet printing as an efficient and flexible alternative fabrication method for printed memristive devices.

Layer Characterization

After the sequential deposition and treatment of the layers (see Experimental Section), the active area of the Ag/a-TiO_2/Ag device is characterized. **Figure 2**a and **Figure 2**b show the active areas of two devices that differ in active layer thickness. Notably, when the thickness of the

resulting a-TiO_2 film is within the range of 50 to 120 nm, it is mainly crack-free (**Figure 2a**). However, when the active layer is thicker than 120 nm the incidence of fissure formation, and consequent damage to the device, increases significantly. These cracks and deformations are also evident in the Ag top layer (**Figure 2b**). **Figure 2**c presents the cross-section SEM image of a printed device, the layers of which have been deposited on a polymer-coated conductive Si (p-doped wafer substrate) for the purpose of SEM imaging. The printed layers and their thicknesses are shown in the inset of **Figure 2**c, and the Pt-EBID and Pt-IBID protective layers are depicted in purple. The Ag layers present porous areas that do not seem to deteriorate the electrical properties in the present application. The active a-TiO_2 layer appears denser and, in general, the printed films are uniform and homogeneously spread on the substrate. **Figure 2**d depicts the relation between layer thickness and prevalence of cracks observed in all of the developed devices. When the thickness of the active layer is below 120 nm (green area of Figure 2d) doesn't appear to have any cracks, however in higher thicknesses between 120 nm-150 nm (green – orange area), the layer starts to deform and finally generate fissures at thicknesses over 150 nm ('spikes' in orange area). Here, the temperature does not appear to promote the formation or healing of cracks and they are solely thickness dependent, as, even when annealed at higher temperatures (130-200 °C) and for longer (2 to 3 hours), active layer morphology was largely unaltered.

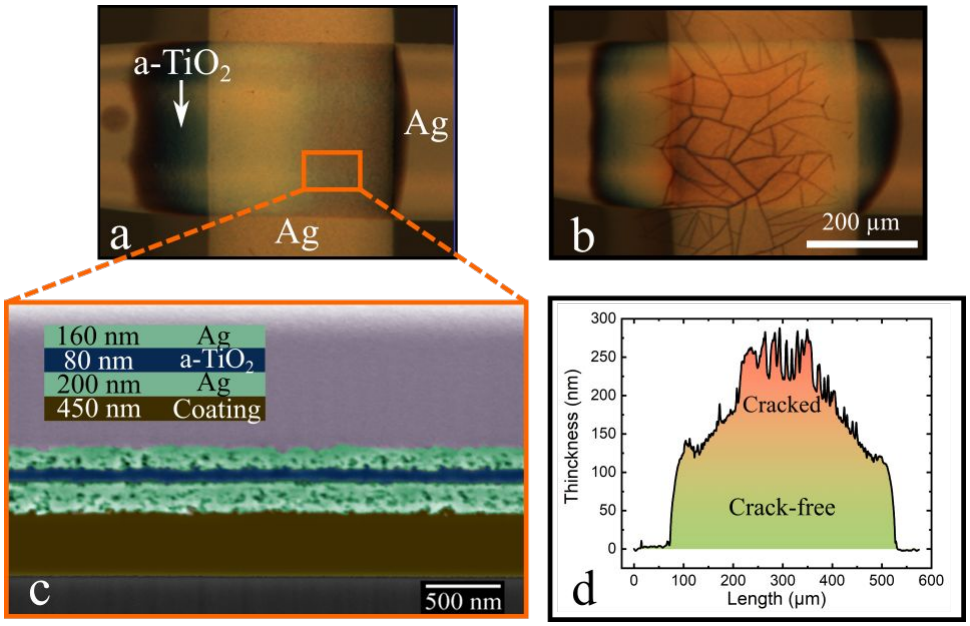

Figure 2. Micrographs of printed polymer coating/Ag/a-TiO_2/Ag devices on glass without (a) and with cracks (b). c) SEM cross-section view of device layers deposited on Si wafer. d) Profilometer results, present the relation between active layer thickness and cracks prevalence.

Overall, both active layer and electrode deposition, along with film formation are well-controlled through the inkjet printing process. This demonstrates that, the critical challenges of crack formation, layer thickness and areal uniformity, and cell-to-cell variability can be effectively managed in fully-printed device structures.

Electrical Characterization

The switching characteristics are investigated by applying voltage pulse-trains to the device and measuring the current output over time. The trigger's timing characteristics of period T (t_{pulse} + t_{int}) and duty cycle α (t_{pulse} / T) are altered, while the amplitude (V_{set}) is fixed at +1 V for all the measurements (see **Figure 3** inset). A voltage withdrawal of 60 s (V_{off}) follows a sequence of

pulse-train in order to investigate the device's capability of resistance state retention. Here, the measurements of *Pulse Train 1* (α ~ 70 %, T = 70 ms) and *Pulse Train 2* (α ~ 70 %, T = 7 ms) are presented. Additional measurements can be found in the Supporting Information (Figure S5, **Figure S6**, **Table S2**). The defining properties for a memristive device in terms of its plasticity is how the output current evolves in relation to the history of events, in this case the pulse trigger timing characteristics.

Initially, *Pulse Train 1* is applied to the device under ambient conditions. **Figure 3** depicts the switching characteristics of the pristine device. An abrupt increase in current takes place, that reaches ~ 4.5×10^{-4} A, followed by a steep and then slow decrease. The observed current overshoot presents spike-like behavior that can be described as analogous to the biological synapse's power-law decay of calcium concentration (Ca^{2+}).[6,51,52] Here, the decay constant τ is approximately 0.5 s. In biological synapses it is often observed that during tetanus (persistent stimuli - train of impulses), the transmission of substances rise briefly due to facilitation before a depression takes place.[53] The depression on initial stage of transmission suggests that it is due to limited store of releasable neurotransmitter (that likely reflects a depletion of a release-ready pool of vesicles) which is exhausted and not instantaneously replenish. It is believed that the most easily released quanta are secreted first, while those remaining are less easily released.[54,55] In general, a decline in post-synaptic current amplitude during repeated stimulation usually is observed, that takes seconds to minutes to recover after stimulation.[56] In c-TiO_2 during the initial electroforming step, a current decay is mainly observed that usually implies heat generation and is believed to be attributed to the formation of a conductive path.[57–59] The present observation lead us to assume that a type of electroforming still occurs in

amorphous phase. This could be ascribed to the development of an intrinsic thermal effect that builds up during the initial voltage application.[60]

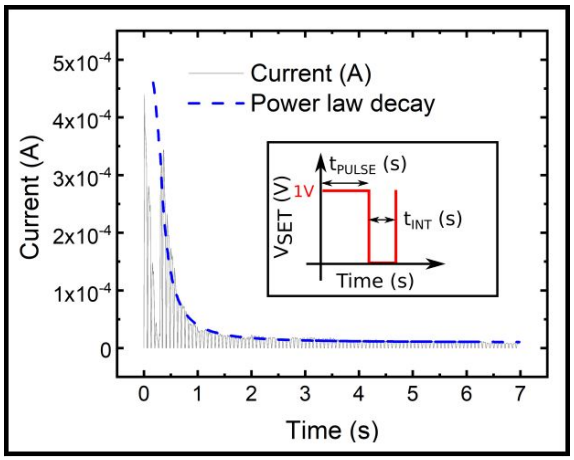

Figure 2. Initial current overshoot of the pristine device under *Pulse Train 1*. Inset: Schematic of pulse trigger timing.

After the current outbreak, the device returns to the high resistance state without showing further conductive characteristics with the given input characteristics. To further investigate the thermal effect on the switching, a temperature of 100 °C is applied to the substrate holder during the remaining electrical measurements of the first device. **Figure 4**a shows the evolution of current over time under *Pulse Train 1* and *Pulse Train 2* including the intermediate 60 s voltage interruptions (V_{off}) that are presented as breaks in the time axis (the original graph can be found in Supporting Information, **Figure S**3). From the observation of the electrical measurements (**Figure 4**a), it can be stated that the device retains its resistance state after V_{off}, thus indicating long-term potentiation (LTP).

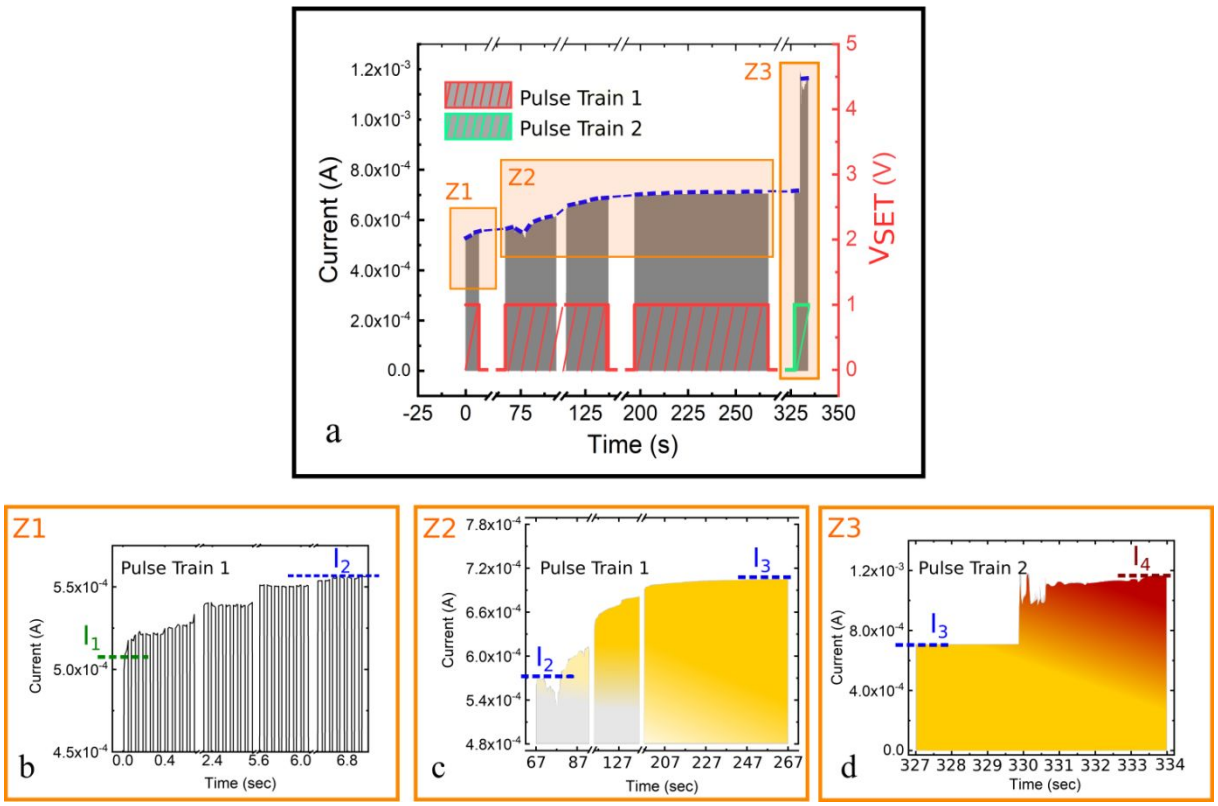

Figure 3. Electrical characterization under 100 °C during *Pulse Train 1* & *Pulse Train 2* triggers. a) Evolution of current over time. b-d) The areas of interest Z1-Z3 of graph (a).

At first, under 100 °C, in the Z1 area of interest in **Figure 4a**, the *Pulse Train 1* is applied for 7 s followed by a V_{off}. In **Figure 4**b it can be seen that a soft, step-wise increase in current by ~ 0.57×10^{-4} A (approx. 10%) occurs and reaches 5.57×10^{-4} A (I_2) (For the full graph see Supporting Information, **Figure S**4). Next, in the Z2 period, the same stimulus continues for a longer period of 200 s. The subsequent current output and intermediate V_{off}, are presented in **Figure 4**c. Initially, the current takes 30 s and then 40 s to increase total by 0.57×10^{-4} A, the same amount as in the primary Z1 case. Finally, it takes more than 60 s to rise by just 50 % of the initial state and reach ~ 7×10^{-4} A (I_3). This observation implies that after the first current increase in Z1 (I_2), a

longer time is required for further augmentation by the same amount. Notably, this is a considerable biomimetic attribute. According to Bi et al.,[61] a significant long-term potentiation (LTP) can be achieved only in synapses with low initial strength, consequently affecting the evolution of the synaptic strength in a non-linear manner, an effect that is usually referred as "metaplasticity".[62] In both biological synapses and in the present electronic synapse, the susceptibility to potentiation is strongly affected by the initial strength or, in other words, the primary resistance state. The lower the resistance state, the greater the potentiation that can be achieved with a given trigger. After the highest current state (in this case, I_3 in Z2 area) is reached, it seems to be sustained regardless of trigger duration. Thus, further change under the same applied stimulus cannot be induced.

Next, after the last V_{off}, *Pulse Train 2* is applied. The measurement results in **Figure 4**d show that the I3 current state of ~ 7×10^{-4} A persists for approximately 3 s and then grows sharply by 3×10^{-4} A, and finally expands to 11.6×10^{-4} A after 7 s (I_4 in Z3 area, **Figure 4**d). Here, the shorter trigger period of *Pulse Train 2* prompts a significant current enhanced. From the current observations it can be stated that during the application of *Pulse Train 1*, the resistance state alters in a slow and step-wise manner until reaching its maximum for the given trigger (I_3). However, during *Pulse Train 2*, where tetanic stimulation is applied, the rate of resistance change is considerably affected, enabling further potentiation in an abrupt, hard switching manner.

Notably, when t_{int} is equal to t_{pulse} (α = 50 %) a reduction in current is observed, with a shorter T again inducing a higher rate of change (see in Supporting Information, **Figure S**6, and **Table S**2).

In this case of a smaller duty cycle, the device recovers from the tetanic stimulation and passes to its relaxation state, consequently the potentiation is hindered. This is comparable to biological synaptic inhibition.[63]

From the electrical characterization, it could be inferred that an additional intrinsic thermal effect may play a driving role in the rate of switching. The following electrical characterization of the second device (see Experimental Section) which is tested under ambient conditions (~ 25 °C) further reinforces this argument. In the second device, initially a V_{set} of α = 78 % with T = 8 s is applied. As **Figure 5**a shows, the output current rises by two orders of magnitude after ~ 100 s of stimulation. After the 60 s V_{off}, α is decreased to 55 % and T to 1 s. **Figure 5**b shows that the current is augmented by one order of magnitude within 7 s, with a further five-fold increase after 10 s.

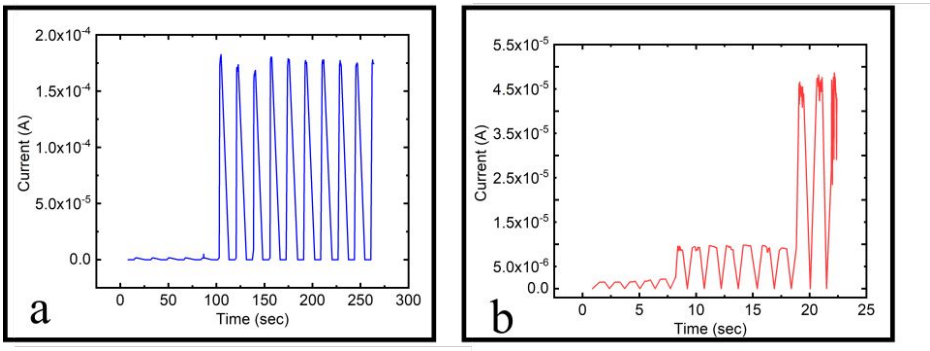

Figure 5. Second device electrical characterization in room temperature under pulse train trigger of: a) α= 78 % and T= 8 s, and after 60 s V_{off} under b) α= 55 % and T= 1 s

These results indicate both a switching behavior with discernible intermediate states (soft switching), and with longer t_{pulse}, a strong facilitation with abrupt increase (hard switching). In

contrast with the first device, after V_{off}, the current do not remain on the same level but reclaims its initial minimum state of ~ 1.5×10^{-6} A. Thus, in this case where external heating is not applied, the device's response follows the electrical frame of short-term potentiation (STP).[64]

To summarize, the synaptic efficacy *(w)* or resistance state, in the present printed Ag/a-TiO_2/Ag devices is strongly affected by the period (T) of the trigger stimuli and the duration of the trigger pulse (t_{pulse}) in relation to the interpulse time (t_{int}). By keeping the voltage amplitude constant at +1V and altering the pulse timing characteristics, transitions to different resistance states can be achieved in an event-driven manner. Tetanic stimulation seems to affect the electronic synapse in the same way as in biological systems. In the case of LTP, the switching threshold is dependent on the prior stimuli applied, an observation that indicates commonalities with the non-linear effect of metaplasticity. Both potentiation and depression (see Supporting Information, **Figure S**6) within a single memristive unit cell, are demonstrated as potentially feasible in fully printed a-TiO_2 electronic synapses. In general, the present findings indicate an activity-dependent modulation of the resistance state with notable biomimetic characteristics.[61,65] Coexistence of both potentiation and depression attributes in a single electronic element enables power efficient electronic systems with brain-inspired and even cognitive functionalities.

Due to the amorphous nature of the derived active layer, the determination of the synapses' underlying switching mechanism is not straightforward. Even in the case of well-known crystalline forms of TiO_2, the exact nature of the switching still constitutes ongoing research.

Here, the most suitable explanation of the conduction is its correlation with the presence of ionic defects, such as impurities, Ti interstitials and V_o. The neutral V_o are deep donors in a-TiO_2.[32] and in the present devices the vacancies are abundant, as can be derived from XPS results. The initial behaviour in Figure 3 could be connected to the movement of the existing electrons. In which case the applied electric field is not enough to stimulate the V_o that instead might act as trapping centres[66] and induce the current decay. The electrical behavior under high temperature is more possibly attributed to ionic movements (in this case Vo) that are likely becoming more mobile than cations[67] and control the switching, inducing LTP (Figure 4). Both intrinsic (with tetanic or strong stimulation) and extrinsic (with external heating) thermal effects seem to influence the switching considerably.

CONCLUSIONS

A low-cost electronic synapse with low electroforming voltage and event-driven attributes is realized by implementing minimal synthesis and a fully additive fabrication process. Device current output is controlled through trigger pulse rate and pulse - interpulse durations, while the amplitude remains at the low level of +1 V. Long-term and short-term potentiation in a single printed cell appear to be possible, enabling versatile operations. An indication of synaptic depression is also observed, suggesting complete bio-emulation. Devices are fabricated by implementing an a-TiO_2 nanoparticle ink developed in-house and optimized, overcoming cracked layers and nozzle clogging, and considerably improving ink lifetime. Since active material robustness has not been previously reported as a critical parameter for fabrication, we can state that the printed memristive devices are still under incipient development and the

present work presents promising results towards fully printed memristive elements. Further improvement of these minimally-structured memristive elements could result in efficient flexible electronic synapses that provide a biomimetic versatile processing system within a single printed unit cell.

ASSOCIATED CONTENT

Supporting Information. The following files are available free of charge.

DLS results of EG-based ink, XPS analysis details and table of elements atomic concentrations, Figure 4a and Figure 4b original graphs, Pulse Train 3 timing characteristics, electrical characterization under Pulse Train 2 to 5, table of Pulse Trains timing characteristics (doc)

AUTHOR INFORMATION

Corresponding Author

*e-mail: v.salonikidou@surrey.ac.uk

Author Contributions

All authors contributed to the manuscript and have given approval to the final version.

Funding Sources

This work is supported in part by the EPSRC (Grant Ref.: EP/P02579X/1) and Altro Ltd.

Notes

The authors declare no conflict of interest.

ACKNOWLEDGMENT

The authors would also like to thank Dr Steven Hinder for the XPS measurements, Mr. You Matsuura for his help with operating the dispenser and Mr. Mateus G. Masteghin for his assistance on SEM measurement.

REFERENCES

(1) Bliss, T. V; Collingridge, G. L. A Synaptic Model of Memory: Long-Term Potentiation in the Hippocampus. *Nature* **1993**, *361* (6407), 31–39. https://doi.org/10.1038/361031a0.

(2) Bi, G. Q.; Poo, M. M. Distributed Synaptic Modification in Neural Networks Induced by Patterned Stimulation. *Nature* **1999**, *401* (6755), 792–796. https://doi.org/10.1038/44573.

(3) Hennig, M. H. Theoretical Models of Synaptic Short Term Plasticity. *Front. Comput. Neurosci.* **2013**, *7*, 45. https://doi.org/10.3389/fncom.2013.00045.

(4) Bliss, J. C.; Crane, H. D.; Mansfield, P. K.; Townsend, J. T. Information Available In Brief Tactile Presentations. *Percept. Psychophys.* **1966**, *1* (4), 273–283. https://doi.org/10.3758/BF03207391.

(5) Zhang, W.; Li, H.; Yang, M.; Mesgarani, N. SYNAPTIC DEPRESSION IN DEEP NEURAL NETWORKS FOR SPEECH PROCESSING. *Proc. ... IEEE Int. Conf. Acoust. Speech, Signal Process. ICASSP* **2016**, *2016*, 5865–5869. https://doi.org/10.1109/ICASSP.2016.7472802.

(6) Graupner, M.; Brunel, N. Calcium-Based Plasticity Model Explains Sensitivity of Synaptic Changes to Spike Pattern, Rate, and Dendritic Location. *Proc. Natl. Acad. Sci.* **2012**, *109*

(10), 3991–3996. https://doi.org/10.1073/pnas.1109359109.

(7) Vitureira, N.; Goda, Y. The Interplay between Hebbian and Homeostatic Synaptic Plasticity. *J. Cell Biol.* **2013**, *203* (2), 175–186. https://doi.org/10.1083/jcb.201306030.

(8) Chua, L. Resistance Switching Memories Are Memristors. *Appl. Phys. A Mater. Sci. Process.* **2011**, *102* (4), 765–783. https://doi.org/10.1007/s00339-011-6264-9.

(9) Chua, L. O. Memristor—The Missing Circuit Element. *IEEE Trans. Circuit Theory* **1971**, *18* (5), 507–519. https://doi.org/10.1109/TCT.1971.1083337.

(10) Jameson, J. R.; Gilbert, N.; Koushan, F.; Saenz, J.; Wang, J.; Hollmer, S.; Kozicki, M. N. One-Dimensional Model of the Programming Kinetics of Conductive-Bridge Memory Cells. *Appl. Phys. Lett.* **2011**, *99* (6), 063506. https://doi.org/10.1063/1.3623485.

(11) Russo, U.; Kamalanathan, D.; Ielmini, D.; Lacaita, A. L.; Kozicki, M. N. Study of Multilevel Programming in Programmable Metallization Cell (PMC) Memory. *IEEE Trans. Electron Devices* **2009**, *56* (5), 1040–1047. https://doi.org/10.1109/TED.2009.2016019.

(12) Indiveri, G.; Linares-Barranco, B.; Legenstein, R.; Deligeorgis, G.; Prodromakis, T. Integration of Nanoscale Memristor Synapses in Neuromorphic Computing Architectures. **2013**. https://doi.org/10.1088/0957-4484/24/38/384010.

(13) Strukov, D. B.; Snider, G. S.; Stewart, D. R.; Williams, R. S. The Missing Memristor Found. *Nature* **2008**, *453* (7191), 80–83. https://doi.org/10.1038/nature06932.

(14) Reyes-Coronado, D.; Rodr??guez-Gattorno, G.; Espinosa-Pesqueira, M. E.; Cab, C.; De Coss, R.; Oskam, G. Phase-Pure TiO2 Nanoparticles: Anatase, Brookite and Rutile. *Nanotechnology* **2008**, *19* (14). https://doi.org/10.1088/0957-4484/19/14/145605.

(15) Mahshid, S. Synthesis of TiO2 Nanoparticles by Hydrolysis and Peptization of Titanium

Isopropoxide Solution . J Mater Process Technol 9 : 65-68. **2007**, *189* (September 2015), 65–68. https://doi.org/10.1016/j.jmatprotec.2007.01.040.

(16) Kim, J. Y.; Kim, S. H.; Lee, H. H.; Lee, K.; Ma, W.; Gong, X.; Heeger, A. J. New Architecture for High-Efficiency Polymer Photovoltaic Cells Using Solution-Based Titanium Oxide as an Optical Spacer. *Adv. Mater.* **2006**, *18* (5), 572–576. https://doi.org/10.1002/adma.200501825.

(17) Mitra, A.; De, G. Sol-Gel Synthesis of Metal Nanoparticle Incorporated Oxide Films on Glass. *Glas. Nanocomposites Synth. Prop. Appl.* **2016**, 145–163. https://doi.org/10.1016/B978-0-323-39309-6.00006-7.

(18) Acharyya, D.; Hazra, A.; Bhattacharyya, P. A Journey towards Reliability Improvement of TiO2based Resistive Random Access Memory: A Review. *Microelectron. Reliab.* **2014**, *54* (3), 541–560. https://doi.org/10.1016/j.microrel.2013.11.013.

(19) Park, S.; Kim, C. H.; Lee, W. J.; Sung, S.; Yoon, M. H. Sol-Gel Metal Oxide Dielectrics for All-Solution-Processed Electronics. *Mater. Sci. Eng. R Reports* **2017**, *114*, 1–22. https://doi.org/10.1016/j.mser.2017.01.003.

(20) Kaltenbrunner, M.; Sekitani, T.; Reeder, J.; Yokota, T.; Kuribara, K.; Tokuhara, T.; Drack, M.; Schwödiauer, R.; Graz, I.; Bauer-Gogonea, S.; Bauer, S.; Someya, T.;Schwo, R. An Ultra-Lightweight Design for Imperceptible Plastic Electronics. *Nature* **2013**, *499* (7459), 458–463. https://doi.org/10.1038/nature12314.

(21) Gale, E.; Pearson, D.; Kitson, S.; Adamatzky, A.; De Lacy Costello, B. The Effect of Changing Electrode Metal on Solution-Processed Flexible Titanium Dioxide Memristors. *Mater. Chem. Phys.* **2015**, *162*, 20–30.

https://doi.org/10.1016/j.matchemphys.2015.03.037.

(22) Gale, E.; Pearson, D.; Kitson, S.; Adamatzky, A.; De Lacy Costello, B. Aluminum Electrodes Effect the Operation of Titanium Oxide Sol-Gel MR. *Mater. Chem. Phys.* **2015**, *162* (May), 20–30. https://doi.org/10.1016/j.matchemphys.2015.03.037.

(23) Vilmi, P.; Nelo, M.; Voutilainen, J.-V.; Palosaari, J.; Pörhönen, J.; Tuukkanen, S.; Jantunen, H.; Juuti, J.; Fabritius, T. Fully Printed Memristors for a Self-Sustainable Recorder of Mechanical Energy. *Flex. Print. Electron.* **2016**, *1* (2), 025002. https://doi.org/10.1088/2058-8585/1/2/025002.

(24) Bhore, S. S. Formulation and Evaluation of Resistive Inks for Applications in Printed Electronics. **2013**, 1–94. https://doi.org/10.1002/adma.201101328.

(25) Nallan, H. C.; Sadie, J. A.; Kitsomboonloha, R.; Volkman, S. K.; Subramanian, V. Systematic Design of Jettable Nanoparticle-Based Inkjet Inks: Rheology, Acoustics, and Jettability. *Langmuir* **2014**, *30* (44), 13470–13477. https://doi.org/10.1021/la502903y.

(26) Tuladhar, T. Measurement of Complex Rheology and Jettability of Inkjet Inks. In *Handbook of Industrial Inkjet Printing: A Full System Approach*; Zapka, W., Ed.; Wiley-VCH Verlag GmbH & Co. KGaA., 2017; pp 409–431.

(27) Chen, X.; Mao, S. S. Titanium Dioxide Nanomaterials: Synthesis, Properties, Modifications and Applications. *Chem. Rev.* **2007**, *107* (7), 2891–2959. https://doi.org/10.1021/cr0500535.

(28) Nagpal, V. J.; Davis, R. M.; Desu, S. B. Novel Thin Films of Titanium Dioxide Particles Synthesized by a Sol-Gel Process. *J. Mater. Res.* **2011**, *10* (12), 3068–3078. https://doi.org/10.1557/JMR.1995.3068.

(29) Savel'ev, S. E.; Alexandrov, A. S.; Bratkovsky, A. M.; Stanley Williams, R. Molecular Dynamics Simulations of Oxide Memory Resistors (Memristors). *Nanotechnology* **2011**, *22* (25), 254011. https://doi.org/10.1088/0957-4484/22/25/254011.

(30) Kim, S.; Jeong, H. Y.; Kim, S. K.; Choi, S. Y.; Lee, K. J. Flexible Memristive Memory Array on Plastic Substrates. *Nano Lett.* **2011**, *11* (12), 5438–5442. https://doi.org/10.1021/nl203206h.

(31) Wouters, D. J.; Waser, R.; Wuttig, M. Phase-Change and Redox-Based Resistive Switching Memories. *Proc. IEEE* **2015**, *103* (8), 1274–1288. https://doi.org/10.1109/JPROC.2015.2433311.

(32) Pham, H. H.; Wang, L. W. Oxygen Vacancy and Hole Conduction in Amorphous TiO2. *Phys. Chem. Chem. Phys.* **2015**, *17* (1), 541–550. https://doi.org/10.1039/c4cp04209c.

(33) Jeong, H. Y.; Lee, J. Y.; Choi, S. Y.; Kim, J. W. Microscopic Origin of Bipolar Resistive Switching of Nanoscale Titanium Oxide Thin Films. *Appl. Phys. Lett.* **2009**, *95* (16), 1–4. https://doi.org/10.1063/1.3251784.

(34) Robertson, J. High Dielectric Constant Gate Oxides for Metal Oxide Si Transistors. *Reports Prog. Phys.* **2006**, *69* (2), 327–396. https://doi.org/10.1088/0034-4885/69/2/R02.

(35) Lanza, M.; Wong, H. S. P.; Pop, E.; Ielmini, D.; Strukov, D.; Regan, B. C.; Larcher, L.; Villena, M. A.; Yang, J. J.; Goux, L.; Belmonte, A.; Yang, Y.; Puglishi, F.M.; Kang, J.; Magyari-Köpe, B.; Yalon, E.; Kenyon, A.; Buckwell, M.; Mehonic, A.; Shluger, A.; Li, H.; Hou, T. H.; Hudec, B.; Akinwande, D.; Ge, R.; Ambrogio, S.; Roldan, J. B.; Miranda, E.; Suñe, J.; Pey, K. L.; Wu, X.; Raghavan, N.; Wu, E.; Lu, W. D.; Navarro, G.; Zhang, W.; Wu, H.; Li, R.; Holleitner, A.; Wurstbauer, U.; Lemme, M. C.; Liu, M.; Long, S.; Liu, Q.; Lv, H.;

Padovani, A.; Pavan, P.; Valov, I.; Jing, X.; Han, T; Zhu, K.; Chen, S.; Hui, F.; Shi, Y. Recommended Methods to Study Resistive Switching Devices. *Adv. Electron. Mater.* **2019**, *5* (1), 1–28. https://doi.org/10.1002/aelm.201800143.

(36) Takeda, Y.; Sekine, T.; Shiwaku, R.; Murase, T.; Matsui, H.; Kumaki, D.; Tokito, S. Printed Organic Complementary Inverter with Single SAM Process Using a P-Type D-A Polymer Semiconductor. *Appl. Sci.* **2018**, *8* (8), 1331. https://doi.org/10.3390/app8081331.

(37) Hench, L. L.; Orefice, R. Sol–Gel Technology. In *Kirk-Othmer Encyclopedia of Chemical Technology*; John Wiley & Sons, Inc.: Hoboken, NJ, USA, 2000. https://doi.org/10.1002/0471238961.19151208051403.a01.

(38) Danks, A. E.; Hall, S. R.; Schnepp, Z. The Evolution of "sol-Gel" Chemistry as a Technique for Materials Synthesis. *Mater. Horizons* **2016**, *3* (2), 91–112. https://doi.org/10.1039/c5mh00260e.

(39) Gergel-Hackett, N.; Hamadani, B.; Dunlap, B.; Suehle, J.; Richter, C.; Hacker, C.; Gundlach, D. A Flexible Solution-Processed Memristor. *IEEE Electron Device Lett.* **2009**, *30* (7), 706–708. https://doi.org/10.1109/LED.2009.2021418.

(40) Abunahla, H.; Mohammad, B.; Applications, S.; Circuits, A. Synthesis and Characterization of Micro-Thick TiO 2 and HfO 2 Memristors. **2018**.

(41) Jang, D.; Kim, D.; Moon, J. Influence of Fluid Physical Properties on Ink-Jet Printability. *Langmuir* **2009**. https://doi.org/10.1021/la900059m.

(42) Li, J.; Rossignol, F.; Macdonald, J. Inkjet Printing for Biosensor Fabrication: Combining Chemistry and Technology for Advanced Manufacturing. *Lab Chip* **2015**, *15* (12), 2538–2558. https://doi.org/10.1039/c5lc00235d.

(43) Chuang, M. Y. Inkjet Printing of Ag Nanoparticles Using Dimatix Inkjet Printer, No 1. **2017**, No. 1.

(44) Diebold, U.; Madey, T. E. TiO 2 by XPS . *Surf. Sci. Spectra* **2002**. https://doi.org/10.1116/1.1247794.

(45) Zanoni, R.; Righini, G.; Montenero, A.; Gnappi, G.; Montesperelli, G.; Traversa, E.; Gusmano, G. XPS Analysis of Sol-gel Processed Doped and Undoped TiO2 Films for Sensors. *Surf. Interface Anal.* **1994**. https://doi.org/10.1002/sia.740220182.

(46) Prusakova, V.; Collini, C.; Nardi, M.; Tatti, R.; Lunelli, L.; Vanzetti, L.; Lorenzelli, L.; Baldi, G.; Chiappini, A.; Chiasera, A.; Ristic, D.; Verucchi, R.; Bortolotti, M.; Dirè, S. The Development of Sol-Gel Derived TiO2thin Films and Corresponding Memristor Architectures. *RSC Adv.* **2017**, *7* (3), 1654–1663. https://doi.org/10.1039/c6ra25618j.

(47) Gale, E. TiO2-Based Memristors and ReRAM: Materials, Mechanisms and Models (a Review). *Semicond. Sci. Technol.* **2014**, *29* (10). https://doi.org/10.1088/0268-1242/29/10/104004.

(48) Thompson, W. A.; Perier, C.; Maroto-Valer, M. M. Systematic Study of Sol-Gel Parameters on TiO2 Coating for CO2 Photoreduction. *Appl. Catal. B Environ.* **2018**, *238* (March), 136–146. https://doi.org/10.1016/j.apcatb.2018.07.018.

(49) Dongale, T. D.; Desai, N. D.; Khot, K. V.; Volos, C. K.; Bhosale, P. N.; Kamat, R. K. An Electronic Synapse Device Based on TiO_2 Thin Film Memristor. *J. Nanoelectron. Optoelectron.* **2018**, *13* (1), 68–75. https://doi.org/10.1166/jno.2018.2297.

(50) Zapka, W. *Handbook of Industrial Inkjet Printing: A Full System Approach*; 2017; Vol. 1–2. https://doi.org/10.1002/9783527687169.

(51) Rubin, D. C.; Hinton, S.; Wenzel, A. The Precise Time Course of Retention. *J. Exp. Psychol. Learn. Mem. Cogn.* **1999**, *25* (5), 1161–1176. https://doi.org/10.1037/0278-7393.25.5.1161.

(52) Kwan, A. C.; Dietz, S. B.; Zhong, G.; Harris-Warrick, R. M.; Webb, W. W. Spatiotemporal Dynamics of Rhythmic Spinal Interneurons Measured With Two-Photon Calcium Imaging and Coherence Analysis. *J. Neurophysiol.* **2010**, *104* (6), 3323–3333. https://doi.org/10.1152/jn.00679.2010.

(53) Hubbard, J. I. Repetitive Stimulation at the Mammalian Neuromuscular Junction, and the Mobilization of Transmitter. *J. Physiol.* **1963**, *169* (3), 641–662. https://doi.org/10.1113/jphysiol.1963.sp007286.

(54) Zucker, R. S. Short-Term Synaptic Plasticity. *Ann. Rev Neusci.* **1989**, *12*, 13–31.

(55) Zucker, R. S.; Regehr, W. G. Short-Term Synaptic Plasticity. *Annu. Rev. Physiol* **2002**, *8* (4), 355–405. https://doi.org/10.1146/annurev.physiol.64.092501.114547.

(56) Del Castillo, J.; Katz, B. Statistical Factors Involved in Neuromuscular Facilitation and Depression. *J. Physiol* **1954**, No. 124, 574–585.

(57) Uenuma, M.; Ishikawa, Y.; Uraoka, Y. Joule Heating Effect in Nonpolar and Bipolar Resistive Random Access Memory. *Appl. Phys. Lett.* **2015**, *107* (7). https://doi.org/10.1063/1.4928661.

(58) Niu, G.; Calka, P.; Auf der Maur, M.; Santoni, F.; Guha, S.; Fraschke, M.; Hamoumou, P.; Gautier, B.; Perez, E.; Walczyk, C.; Wenger, C.; Di Carlo, A.; Alff, L.; Schroeder, T. Geometric Conductive Filament Confinement by Nanotips for Resistive Switching of HfO2-RRAM Devices with High Performance. *Sci. Rep.* **2016**, *6*, 25757.

https://doi.org/10.1038/srep25757.

(59) Yu, S.; Guan, X.; Wong, H. S. P. Understanding Metal Oxide RRAM Current Overshoot and Reliability Using Kinetic Monte Carlo Simulation. *Tech. Dig. - Int. Electron Devices Meet. IEDM* **2012**, 585–588. https://doi.org/10.1109/IEDM.2012.6479105.

(60) Yu, S.; Wu, Y.; Jeyasingh, R.; Kuzum, D.; Wong, H. S. P. An Electronic Synapse Device Based on Metal Oxide Resistive Switching Memory for Neuromorphic Computation. *IEEE Trans. Electron Devices* **2011**, *58* (8), 2729–2737. https://doi.org/10.1109/TED.2011.2147791.

(61) Bi, G.; Poo, M. Synaptic Modifications in Cultured Hippocampal Neurons: Dependence on Spike Timing, Synaptic Strength, and Postsynaptic Cell Type. *J. Neurosci.* **1998**, *18* (24), 10464–10472. https://doi.org/10.1523/JNEUROSCI.18-24-10464.1998.

(62) Abraham, W. C.; Bear, M. F. Metaplasticity: The Plasticity of Synaptic Plasticity. *Trends Neurosci.* **1996**, *19* (4), 126–130. https://doi.org/10.1016/S0166-2236(96)80018-X.

(63) Abraham, W. C.; Bear, M. F. Metaplasticity : Plasticity of Synaptic. *Trends Neurosci* **1996**, *19*, 126–130.

(64) Abbott, L. F.; Regehr, W. G. Synaptic Computation. *Nature* **2004**, *431* (7010), 796–803. https://doi.org/10.1038/nature03010.

(65) Vogels, T. P.; Froemke, R. C.; Doyon, N.; Gilson, M.; Haas, J. S.; Liu, R.; Maffei, A.; Miller, P.; Wierenga, C. J.; Woodin, M. A.; Zenke, F.; Sprekeler, H. Inhibitory Synaptic Plasticity: Spike Timing-Dependence and Putative Network Function. *Front. Neural Circuits* **2013**, *7* (July), 1–11. https://doi.org/10.3389/fncir.2013.00119.

(66) Tao, D.; Chen, J.; Jiang, Z.; Qi, B.; Zhang, K.; Wang, W. Making Reversible Transformation

from Electronic to Ionic Resistive Switching Possible by Applied Electric Field in an Asymmetrical Al/TiO2/FTO Nanostructure. *Appl. Surf. Sci.* **2019**, 144124. https://doi.org/10.1016/j.apsusc.2019.144124.

(67) Waser, R.; Aono, M. <nmat2023 Nanoionics-Based Resistive Switching Memories.Pdf>. **2007**, 833–840. https://doi.org/10.1038/nmat2023.

TOC Graphic

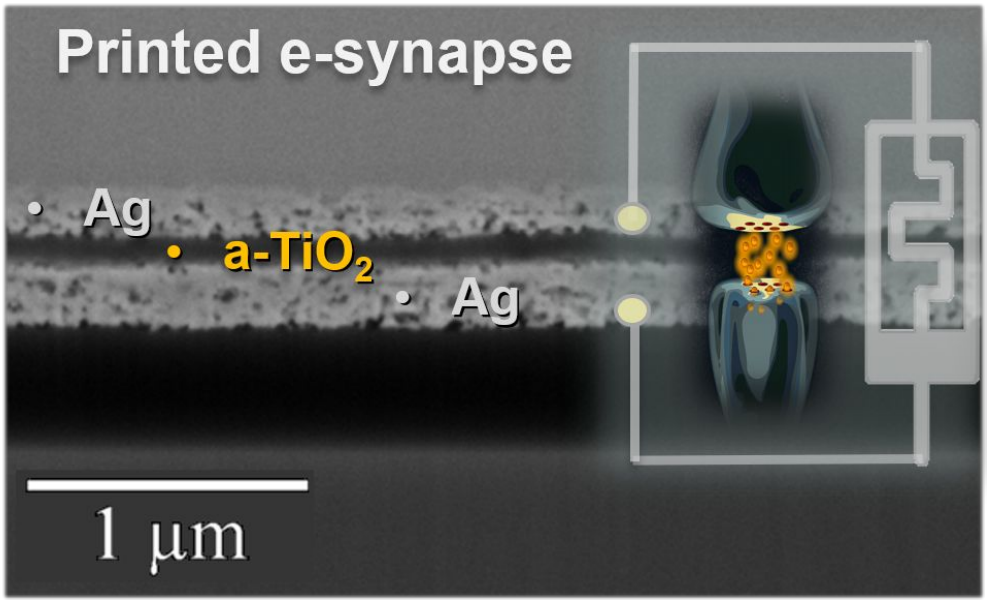

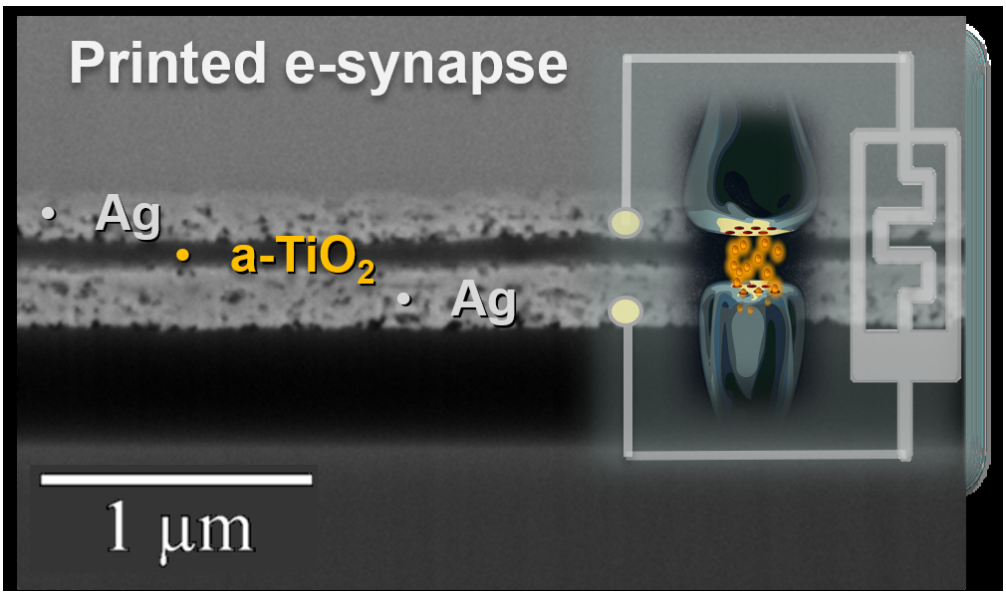

TOC Graphic

106x62mm (240 x 240 DPI)